*J. Fluid Mech.* (2009), *vol.* 633, *pp.* 355–379.  
doi:10.1017/S0022112009007162 Printed in the United Kingdom

# Evolution and breaking of parametrically forced capillary waves in a circular cylinder

BABURAJ A. PUTHENVEETTIL[1]† AND E. J. HOPFINGER[2]

[1]Department of Applied Mechanics, Indian Institute of Technology Madras, Chennai-600 036, India

[2]LEGI-CNRS-UJF, BP 53, 38041 Grenoble Cedex 9, France

(Received 27 July 2008 and in revised form 22 February 2009)

We present results on parametrically forced capillary waves in a circular cylinder, obtained in the limit of large fluid depth, using two low-viscosity liquids whose surface tensions differ by an order of magnitude. The evolution of the wave patterns from the instability to the wave-breaking threshold is investigated in a forcing frequency range ($f = \omega/2\pi = 25$–$100$ Hz) that is around the crossover frequency ($\omega_{ot}$) from gravity to capillary waves ($\omega_{ot}/2 \leqslant \omega/2 \leqslant 4\omega_{ot}$). As expected, near the instability threshold the wave pattern depends on the container geometry, but as the forcing amplitude is increased the wave pattern becomes random, and the wall effects are insignificant. Near breaking, the distribution of random wavelengths can be fitted by a Gaussian. A new gravity–capillary scaling is introduced that is more appropriate, than the usual viscous scaling, for low-viscosity fluids and forcing frequencies $<10^3$ Hz. In terms of these scales, a criterion is derived to predict the crossover from capillary- to gravity-dominated breaking. A wave-breaking model is developed that gives the relation between the container and the wave accelerations in agreement with experiments. The measured drop size distribution of the ejected drops above the breaking threshold is well approximated by a gamma distribution. The mean drop diameter is proportional to the wavelength determined from the dispersion relation; this wavelength is also close to the most likely wavelength of the random waves at drop ejection. The dimensionless drop ejection rate is shown to have a cubic power law dependence on the dimensionless excess acceleration $\epsilon_d'$; an inertial–gravitational ligament formation model is consistent with such a power law.

## 1. Introduction

Wave motions at liquid–gas interfaces, especially wave breaking and drop ejection, can substantially increase the interfacial heat and mass transfer. An example is the mass transfer across the air–sea interface at which gravity and capillary waves play an essential role. Saylor & Handler (1997) showed that capillary waves can increase the transfer rate of $CO_2$ by two orders of magnitude compared with the diffusive flux at an undisturbed interface. Another application is in liquid fuel tanks that are often subjected to vibrations in the frequency ranges corresponding to either gravity or capillary waves; the fuels are usually of low viscosity and have low surface tension with air. When the tanks are exposed to external heat fluxes, the waves at the liquid–gas interface can be the cause of large pressure changes due to enhanced evaporation

† Email address for correspondence: apbraj@iitm.ac.in

or condensation (Hopfinger & Das 2009, Das & Hopfinger 2009). In the kilohertz and the megahertz ranges, the production of sprays by vibrations has been studied rather extensively, but the mechanisms of droplet formation are rather complex and are not well understood (Yule & Al-Suleimani 2000). There are thus fundamental as well as practical interests for studying interfacial waves, including wave breaking and droplet ejection, in the capillary–gravity frequency range (driving frequency $<1$ kHz), especially in low-viscosity fluids with low surface tension.

Well-controlled waves in a container can be produced by forcing the container in the direction normal to the liquid surface. Such waves, known as Faraday waves, that are sub-harmonically excited (wave frequency equal to half the driving frequency) have been extensively studied in both the gravity and the capillary limit (Benjamin & Ursell 1954; Miles & Henderson 1990; Kumar & Tuckerman 1994; Edwards & Fauve 1995; Kudrolli & Gollub 1996). In such waves, the crossover from gravity to capillary waves corresponds to the equality of the gravity and capillary terms in the dispersion relation

$$\omega_o^2 = \left(gk + \frac{\sigma}{\rho}k^3\right)\tanh(kh), \tag{1.1}$$

were $g$ is the gravitational acceleration, $k$ the wavenumber, $\sigma/\rho$ the kinematic surface tension, $h$ the fluid depth and $\omega_o$ the circular wave frequency. The fluid depth can be considered infinite when $\tanh(kh) \cong 1$. According to (1.1), the crossover wave frequency from gravity waves to capillary waves is given by

$$\omega_{ot} = (4g^3\rho/\sigma)^{1/4}. \tag{1.2}$$

The driving threshold acceleration for parametric instability in the capillary, unbounded and infinite fluid depth limits, is

$$a_c = 8(\rho/\sigma)^{1/3}\nu\omega^{5/3} \tag{1.3}$$

(Kumar & Tuckerman 1994; Edwards & Fauve 1995), where the circular driving frequency $\omega = 2\omega_o$ and $\nu$ is the kinematic viscosity.

Experiments on Faraday waves are usually conducted in finite-size containers that makes the wave pattern in low-viscosity fluids dependent on the container geometry (Gollub & Meyer 1983). Sidewall boundary effects are felt to a decay length

$$l_d \sim \sigma/(4\nu\rho\omega) \tag{1.4}$$

so that the container side boundaries can be disregarded only when $R \gg l_d$, where $R$ is the radius of the container; the system is then considered as a 'large system' (Bechhoefer *et al.* 1995; Edwards & Fauve 1995). By analogy with Rayleigh–Bénard convection, the aspect ratio $\zeta = R/h$ is sometimes used to distinguish between large and small devices (Kudrolli & Gollub 1996). While a large aspect ratio may imply that $R/l_d$ is also large, $R/h$ is not the relevant parameter for characterizing lateral boundary effects in the case of Faraday waves. For instance, in applications in which the container radius is very large, $R/h$ is of order 1, whereas $R/l_d \gg 1$.

Beyond the stability limit, the pattern evolution of Faraday waves is complex. Theories that propose three-wave resonant interactions (Chen & Vinals 1997; Zhang & Vinals 1997) in the capillary limit for unbounded fluid layers have been successful in matching experiments in large systems (Kudrolli & Gollub 1996; Binks, Westra & Van de Water 1997) near the instability threshold. No general theory exists for pattern evolution in small systems in which side boundary effects are important. Ciliberto & Gollub (1985) proposed that in small systems the evolution of wave

patterns can be due to mode competition. For water at a forcing frequency $f = 16\,\mathrm{Hz}$ in a container of radius $R = 6.35\,\mathrm{cm}$, these authors showed that this competition can give rise to oscillations at $\omega/2$, a single stable mode, a slow periodic variation or a chaotic variation of amplitudes. Gollub & Meyer (1983) observed that in a container of $R = 2.41\,\mathrm{cm}$, filled with water and forced at $f = 62\,\mathrm{Hz}$, the wave motions become chaotic at $\epsilon = (a - a_c)/a_c$ of about 1, where $a$ is the driving acceleration. All these studies were limited to $\epsilon < 1.37$, well below wave-breaking conditions.

At large amplitudes of vibrations, waves break ejecting drops; far less is known about such large-amplitude waves and wave-breaking conditions. Jiang *et al.* (1996) and Jiang, Perlin & Schultz (1998) demonstrated the breaking scenario of parametrically forced two-dimensional gravity waves. Different breaking scenarios and the chaotic nature of capillary wave breaking has been pointed out by Yule & Al-Suleimani (2000) in experiments on vibration-induced atomization of a thin liquid layer. Goodridge, Shi & Lathrop (1996), Goodridge *et al.* (1997) and Goodridge, Hentschel & Lathrop (1999) determined the drop ejection threshold acceleration for capillary waves in water and glycerine–water mixtures up to driving frequencies of 100 Hz but did not investigate the wave pattern at large $\epsilon$. The critical driving acceleration for the onset of drop ejection given by Goodridge *et al.* (1996, 1997, 1999) is

$$a_d \approx 0.26(\sigma/\rho)^{1/3}\omega^{4/3}, \tag{1.5}$$

which is independent of viscosity in the frequency range of the experiments. Goodridge *et al.* (1997, 1999) introduced capillary–viscous scales in the forms

$$\Omega_\nu = \frac{(\sigma/\rho)^2}{\nu^3} \tag{1.6}$$

for the frequency,

$$L_\nu = \frac{\nu^2}{\sigma/\rho} \tag{1.7}$$

for the length and $a_\nu = L_\nu \Omega_\nu^2$ for the acceleration. In dimensionless form, (1.5) is then written as $a_\nu^* \approx 0.26\,(\omega_\nu^*)^{4/3}$, where

$$a_\nu^* = a/a_\nu \quad \text{and} \tag{1.8}$$

$$\omega_\nu^* = \omega/\Omega_\nu. \tag{1.9}$$

From measurements of the droplet ejection acceleration threshold, Goodridge *et al.* (1997) concluded that capillary wave breaking is independent of viscosity if $\omega_\nu^* \leqslant 10^{-5}$. This has been confirmed by James, Smith & Glezer (2003*a*) and James *et al.* (2003*b*) who conducted experiments on parametric instability of large drops at driving frequencies of about 1000 Hz. From measurements of the ejected drop sizes in the frequency range 1.52–2.42 MHz, Donnelly *et al.* (2004) concluded that viscous effects on the drop diameter are insignificant up to $\omega_\nu^* \sim O(0.1)$. Similar conclusions were reached by the study of drop size distribution due to vibration-induced atomization at around 1 kHz by Vukasinovic, Smith & Glezer (2004). Since viscosity effects are insignificant in low-viscosity fluids, at least at driving frequencies $<1$ kHz, a more appropriate scaling is a gravity–capillary scaling, as will be shown in § 4.1.

For $a > a_d$, Goodridge *et al.* (1999) determined the drop ejection rate

$$\Phi = N/(ST\omega_o) \tag{1.10}$$

and proposed the power law

$$\Phi = 0.039\epsilon_d^{2.8}, \tag{1.11}$$

where $N$ is the number of drops ejected during time $T$ from a projected surface area $S$ of the fluid surface and $\epsilon_d = (a - a_d)/a_d$. The above expression is based only on experiments with one liquid at one driving frequency. It is likely to be incomplete, as it equates a dimensional quantity $\Phi$, which has the dimension of number of drops per unit surface area, to a dimensionless parameter $\epsilon_d$. Further, the drop size distribution of the ejected drops has been measured only in sprays formed by vibrations in the kilohertz and megahertz ranges (Lang 1962; Topp 1973; Donnelly *et al.* 2004; Vukasinovic *et al.* 2004). Whether these results obtained in the megahertz range, where viscous effects are important in the breaking process, are similar to the drop sizes and their distribution at frequencies of the order of $10^2$ Hz is still not known.

In the present paper, we present experimental results of the nonlinear evolution and wave breaking of sub-harmonically excited Faraday waves for frequencies $\omega_{ot}/2 \leqslant \omega/2 \leqslant 4\omega_{ot}$ using low-viscosity fluids of kinematic surface tensions that differ by an order of magnitude. Because of the low viscosity, the decay length is of the order of the container radius. Therefore, the system is a 'small system' with the wave patterns near the instability onset, depending on the container geometry. We show how this pattern evolves from small $\epsilon$ to large $\epsilon$ where the wave motion becomes random and independent of the container geometry; boundary effects are in this case confined to the Stokes layer thickness. The wavelengths at drop ejection are the same as the inviscid dispersion wavelength.

Concerning the drop ejection, the interest of the present results with respect to those of Goodridge *et al.* (1997) is the use of two liquids of widely different surface tensions to validate the proposed models. We used water in air ($\sigma = 72\,\mathrm{dyn\,cm^{-1}}$, $\omega_{ot} = 85\,\mathrm{rad\,s^{-1}}$) and FC-72 in air ($\sigma = 10\,\mathrm{dyn\,cm^{-1}}$, $\omega_{ot} = 158\,\mathrm{rad\,s^{-1}}$); a glycerine–water solution was also used to verify the decay length $l_d$. In addition, we introduce a simple but important new gravity–capillary scaling that is more appropriate for low-viscosity liquids in the frequency range in which viscous effects are insignificant. This scaling gives the transition from capillary- to gravity-dominated breaking; the dimensionless values of the threshold accelerations are of order 1 instead of order $10^{-5}$ when using the viscous scales. Furthermore, a simple breakup model is developed that demonstrates the essential physics of drop ejection. Using this model, a relation between the wave and the container acceleration is obtained; an information that is of interest for interfacial heat and mass transfer models. The measurements of the drop size distribution are the first in the present frequency range. In applications, wall vibrations can be the cause for capillary waves and possible drop ejection. Hence, in appendix A, the drop ejection conditions for horizontally forced capillary waves (horizontal vibrations) are briefly discussed. The results obtained with horizontal forcing confirm the capillary drop ejection model developed. The drop ejection rate has been measured for the two fluids, and a model is proposed that collapses the data reasonably well.

The paper is organized as follows: In § 2 the experimental conditions and the procedures are presented. The observed wave pattern evolution is discussed in § 3. Section 4 contains the results on drop ejection, giving the acceleration threshold in terms of the new gravity–capillary scaling, followed by the breakup model and the relation between the container and the wave acceleration. The drop size measurements are presented in § 4.4. The drop ejection rate is discussed in § 4.5, and the main conclusions given in § 5. In Appendix A, the drop ejection threshold is given for

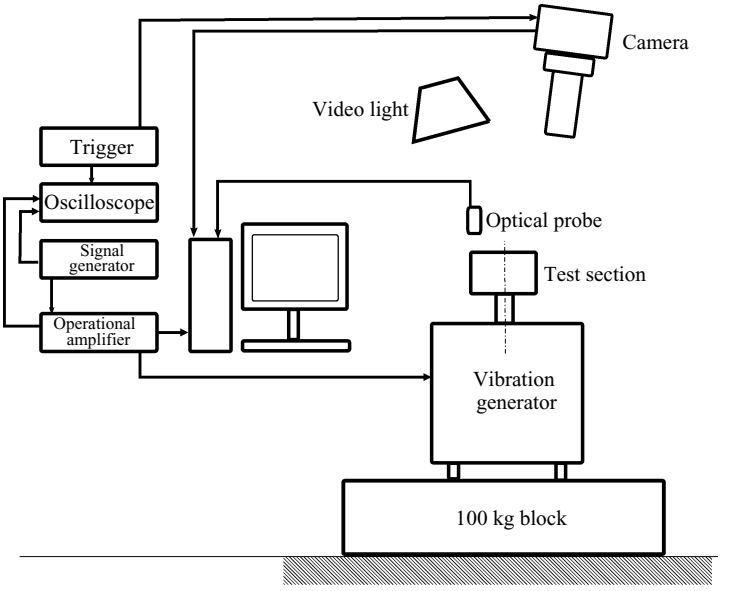


FIGURE 1. The experimental set-up.

horizontal forcing. Appendix B dicusses a simple model for the observed drop ejection rate.

## 2. Experimental conditions

The experimental set-up used was a transparent circular cylinder of radius $R = 2.5$ cm and depth 3 cm, filled with the test fluid and mounted on a Bruel & Kjaer 4809 vibration exciter (figure 1). The vibration exciter was driven by a signal generator through a Bruel & Kjaer 2709 amplifier. The container acceleration is given by $a(t) = A\omega^2 \sin(\omega t)$, where $A$ is the shaker amplitude. The signal generator and the amplifier were electrically isolated so as to output a clean sinusoidal signal into the vibration exciter. To reduce unwanted vibrations, the vibration exciter was bolted to a 100 kg steel block that was placed on a vibration damper sheet.

Water and FC-72 were used in the study as the test fluids. Sufficient care was taken to avoid contaminants in the fluids. We used de-ionized water, fresh samples of which, taken from airtight storages, were used for each experiment. FC-72 (3M 2000) is a clear colourless liquid with low surface tension with air and is fully wetting. The relevant properties of FC-72 are shown in table 1. FC-72, due to its low surface tension in air, is not prone to contamination as much as water. FC-72 was also taken from sealed containers and handled carefully to avoid contamination. In all the cases, the test section was first rinsed with fresh samples before filling the test fluid. The experiments were of short duration, and the samples were not left exposed to atmosphere for long periods. Since $\tanh(kh) \cong 1$ for these fluids for the present set-up, we approximated the system to be of infinite depth. A few experiments to determine the effects of viscosity on the wave patterns and the drop ejection criterion were also conducted with glycerine–water solution.

To reduce the meniscus waves, brimful conditions were maintained for water and glycerine–water solutions. The container was filled to a level at which no deflection in the reflected light beam from the liquid surface was observed at the container edge.

| | $\rho$, (g cm$^{-3}$) | $\nu$, (cm$^2$ s$^{-1}$) | $\sigma$, (dyn cm$^{-1}$) | $a_c/g$ | $\lambda$ (cm) | $l_d$ (cm) | $\omega_{ot}/2\pi$ (Hz) |
|---|---|---|---|---|---|---|---|
| FC-72 | 1.680 | 0.0038 | 10 | 0.0761 | 0.49 | 2.56 | 25.3 |
| Water | 0.997 | 0.0089 | 72.8 | 0.26 | 0.99 | 6.43 | 13.5 |
| Glycerine–water solution | 1.26 | 1.44 | 63 | 46.46 | 0.9 | 0.028 | 14.8 |

TABLE 1. Properties of the fluids used at 20°C taken from Batchelor (1969) for water and from 3M (2000) for FC-72: $\rho$ = density, $\nu$ = kinematic viscosity, $\sigma$ = surface tension in air, $a_c$ = critical acceleration for Faraday instability calculated from (1.3), $\lambda$ = wavelength from dispersion relation (1.1) for infinite depth, $l_d$ = viscous decay length calculated from (1.4); $a_c$, $\lambda$ and $l_d$ are calculated for $f = \omega/2\pi = 50$ Hz. The wavelength for the glycerine–water solution has been calculated from the viscous dispersion relation $\lambda_v = 3\pi\sqrt{\nu/\omega_o}$ given by Donnelly *et al.* (2004).

For FC-72, brimful conditions could not be maintained, because the liquid is volatile and fully wetting. We did not study the effect of volatility on the interface motion in the case of FC-72. Since the liquid and surrounding air temperatures were the same, evaporation occurred until the equilibrium partial vapour pressure was reached above the liquid surface. Evaporation was rapid at the start (during about 10 s) but then was slow and had a negligible effect on the interfacial motion when the forcing amplitude was small. At larger forcing amplitudes when drop ejection occurred, there was generally about 1 mm loss of liquid.

Wave patterns were captured using reflected diffused light from the liquid surface by an overhead digital camera (JAI) with a macro lens. The light source was kept at an angle of about 10° with respect to the vertical at about 1 m above the liquid surface. The camera was also placed at the same angle and height as the light source, as shown in figure 1. This arrangement was found to give the best pictures of the surface waves. The camera was triggered with an external trigger; the wave patterns were frozen by adjusting the trigger frequency. Wave frequency was obtained by viewing the wave patterns at the sub-harmonic frequency and then at the harmonic frequency. The images froze when the trigger frequency was half the driving frequency. When viewed at harmonic trigger frequency, the sub-harmonic waves showed alternating crests and troughs at the same position. To study wave heights, drop diameters and drop ejection rates, side view images were taken after aligning the light source, test section and the camera in a horizontal line, with the camera centre at the height of the liquid surface.

The vibration exciter was calibrated to determine the acceleration for a given amplifier voltage. Using an optical displacement probe pointed at the top solid surface of the container the displacement for different amplifier voltages at three driving frequencies of 25 Hz, 50 Hz and 100 Hz were measured. Calibration plots of root mean square (r.m.s.) input voltages to the amplifier versus the corresponding maximum acceleration of the container were prepared for the three frequencies for the three fluids and used in the calculations. During calibration, the container was filled with the experimental fluid and sealed with tape in order to have the same weight as in the experiments.

## 3. Pattern evolution

Figures 2(*a*) and 2(*b*) show the observed wave patterns when $a < a_c$, where $a_c$ is calculated from (1.3), at a driving frequency of $f = \omega/2\pi = 50$ Hz for FC-72 and glycerine–water solution. The pattern at $f = 100$ Hz for water when $a < a_c$ is shown

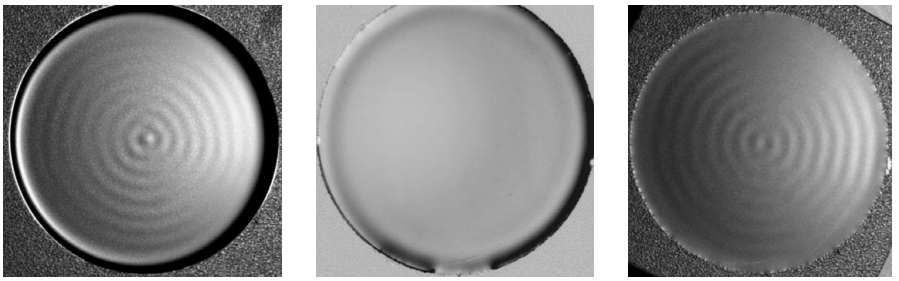

(*a*) (*b*) (*c*)

FIGURE 2. Wave patterns at accelerations $a$ less than the critical acceleration $a_c$ (1.3) for forcing frequency $f = 50$ Hz: (*a*) for FC-72 at $\epsilon = (a - a_c)/a_c = -0.76$; (*b*) for glycerine–water solution at $\epsilon = -0.87$; and (*c*) wave patterns for $f = 100$ Hz at $\epsilon = -0.25$ for water.

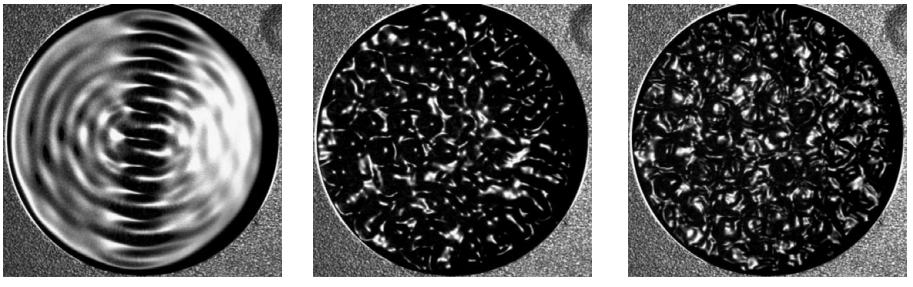

(*a*) (*b*) (*c*)

FIGURE 3. Pattern evolution for $a \gtrsim a_c$ in FC-72 at $f = 50$ Hz. (*a*) Sub-harmonic parametric instability at $\epsilon = -0.17$. The wavelengths are about 1.6 times that of synchronous meniscus waves in figure 2(*a*) as expected from the dispersion relation. (*b*) Instantaneous pattern when random movements of fluid cones occur at $\epsilon = 0.98$. The crests are seen as white spots with the troughs as white lines surrounding the crests. The crests move about randomly over the surface. (*c*) Wave pattern at drop ejection at $\epsilon = 3.14$. The wave slopes steepen, and the crests move faster.

in figure 2(*c*). The waves in figures 2(*a*) and 2(*c*) are synchronous meniscus waves. The decay length for the conditions in figures 2(*a*) and 2(*c*) is of the order of $R$ (see table 1). Hence, meniscus waves, which are synchronous with the forcing, are seen over the whole surface. In the case of water, the container is filled to its upper edge. In spite of this, meniscus waves are generated. Meniscus waves exist for FC-72 even though the kinematic surface tension is very small. As is clear from figure 2(*b*), no meniscus waves are observed for glycerine–water mixture because the decay length is much smaller than $R$. The wavelengths calculated from (1.1) are given in table 1. The contribution of the gravitational term to the wavelength, which depends on the forcing frequency and the surface tension, is small (2.7 % for water to 25 % for FC-72 at $f = 50$ Hz) in the case of low-viscosity liquids. For glycerine–water in the viscous regime, the wavelength given in table 1 has been calculated from $\lambda_v = 3\pi\sqrt{\nu/\omega_o}$ given by Donnelly *et al.* (2004). This value is practically identical to the wavelength calculated from the inviscid dispersion relation (1.1) because the conditions for glycerine–water nearly coincide with the crossover from the capillary to the viscous threshold wavelength (Donnelly *et al.* 2004).

The evolution of wave patterns in FC-72 when $a$ is increased beyond $a_c$ for frequencies of 50 Hz, 100 Hz and 25 Hz is shown in figures 3–5 respectively. In

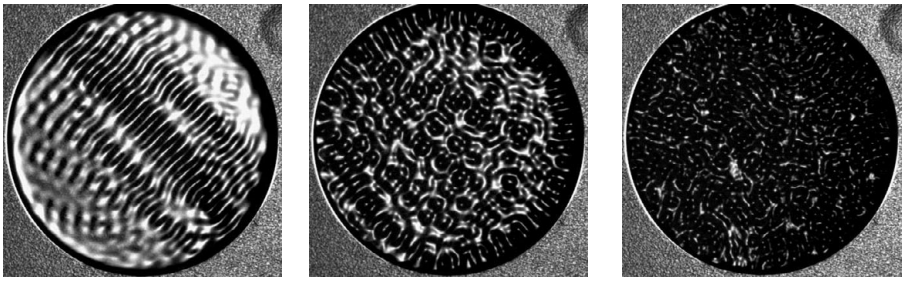

(*a*) (*b*) (*c*)

FIGURE 4. Pattern evolution for $a \gtrsim a_c$ in FC-72 at $f = 100\,\text{Hz}$: (*a*) parametric instability at $\epsilon = -0.31$; (*b*) instantaneous pattern from random movement of fluid cones at $\epsilon = 0.25$; (*c*) wave pattern at drop ejection at $\epsilon = 1.73$.

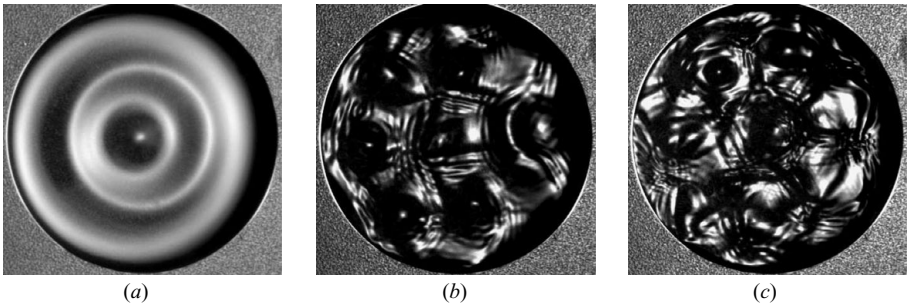

(*a*) (*b*) (*c*)

FIGURE 5. Pattern evolution for $a > a_c$ in FC-72 at $f = 25\,\text{Hz}$ in the gravity–capillary regime. (*a*) Sub-harmonic waves at $\epsilon = 0.14$. Parametric instability in the form of lines are not seen. (*b*) Azimuthal modulation on the circular waves at $\epsilon = 1.2$. (*c*) Pattern at drop ejection at $\epsilon = 4.56$.

figure 3(*a*) at $\epsilon = (a - a_c)/a_c = -0.17$, the parametric instability (at sub-harmonic frequencies) dominates over the initial synchronous meniscus waves (shown in figure 2*a*) and develops parallel lines of steeper slopes. Parametric instability is observed for $a$ slightly less than $a_c$ ($\epsilon = -0.17$) because $a_c$ calculated from (1.3) is valid for idealized conditions. With increasing $\epsilon$, the stripe pattern of the parametric instability breaks down to form laterally moving fluid cones, an instantaneous pattern of which is shown in figure 3(*b*) at $\epsilon = 0.98$. The crests (seen as white spots) and the troughs (seen as thin lines surrounding the crests) move about laterally in a random way. At higher $\epsilon$, the wave slopes steepen; the white spots become points and the lines narrow; the random lateral movements become faster and drops are ejected from the crests. The instantaneous pattern at this stage, when $\epsilon = 3.14$, is shown in figure 3(*c*). A similar route from meniscus waves, giving way to stable parametric waves, that break down to random movements of fluid cones to drop ejection is seen in figure 4 for FC-72 at 100 Hz. The wavelengths here are smaller as expected at a larger forcing frequency. At $f = 25\,\text{Hz}$ parametric instability in the form of lines is not seen. Instead, sub-harmonic circular waves are observed (figure 5*a*). Gravity effects are important in FC-72 at this lower frequency (see table 1), resulting in a larger wavelength and decay length so that the sidewall effects are stronger near the instability threshold. The appearance of an azimuthal modulation to break down the circular wave into circularly arranged peaks and troughs is seen clearly in figure 5. At drop ejection when $\epsilon = 4.56$ in figure 5(*c*), the wave pattern is again more random.

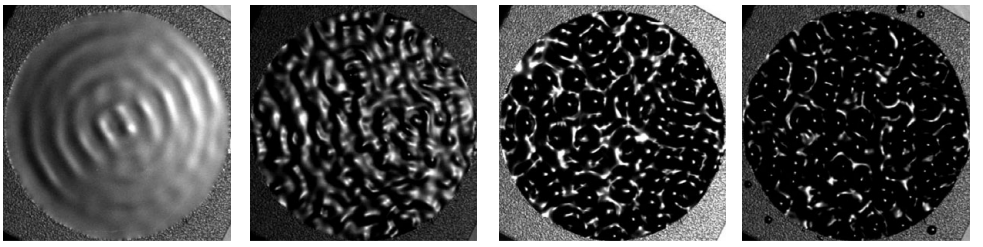

(*a*) (*b*) (*c*) (*d*)

FIGURE 6. Pattern evolution in water at $f = 100$ Hz. (*a*) Parametric instability at $\epsilon = 0.35$. (*b*), (*c*) Instantaneous patterns of the random waves at $\epsilon = 2.35$ and $\epsilon = 4.24$. (*d*) Steepening of slopes and drop ejection at $\epsilon = 5.53$.

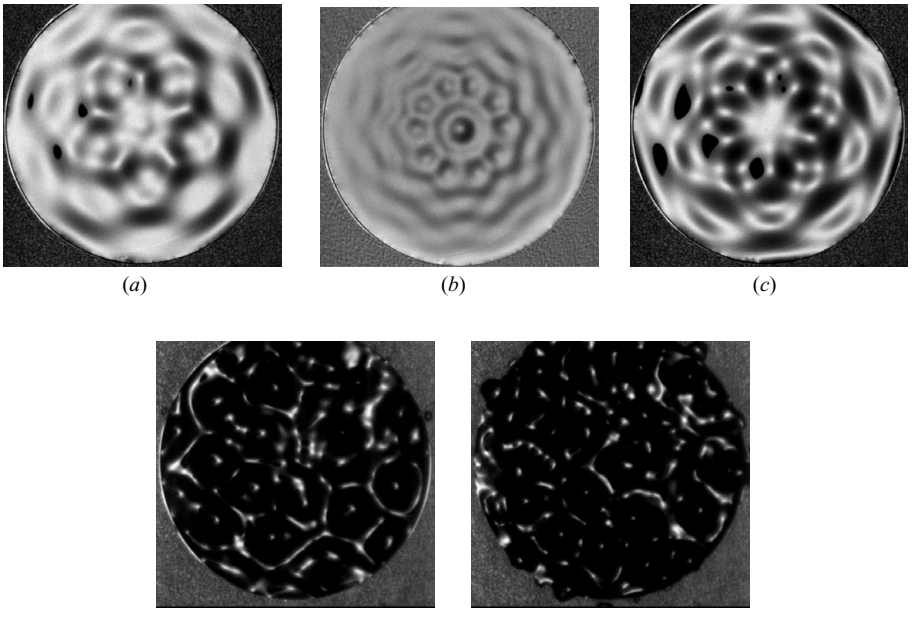

(*a*) (*b*) (*c*)

(*d*) (*e*)

FIGURE 7. Pattern evolution for $a > a_c$ in water at $f = 50$ Hz. (*a*)–(*c*) Cyclic pattern change, with a time period of 38 s (0.026 Hz), at $\epsilon = 1.01$. (*d*) Instantaneous pattern of random lateral wave movements at $\epsilon = 5$. (*e*) Drop ejection at $\epsilon = 9.5$. In (*e*), the wave slopes steepen; the crests move faster.

The pattern evolution in water at 100 Hz (figure 6) is similar to that in FC-72 at 50 Hz and 100 Hz; the wavelengths are larger than that in FC-72 at the same frequency due to the larger kinematic surface tension of water. At $f = 50$ Hz in water, pattern evolution above $a_c$ is different, and an azimuthal modulation of the initial circular wave pattern (similar to that of figure 2*c*) occurs. This modulation gives rise to a periodic pattern change. A typical cyclic change of pattern at $\epsilon = 1.01$ is shown in figures 7(*a*)–7(*c*). The time period of the beat cycle is 38 s. With increasing $\epsilon$, the three patterns in the beat cycle break down to randomly moving cusps and troughs as in the earlier cases; the resulting instantaneous pattern is shown in figure 7(*d*) at $\epsilon = 5$. The dynamics then remain similar to that observed earlier. The cusps and troughs

sharpen and move faster; the instantaneous pattern at drop ejection when $\epsilon = 9.5$ is shown in figure 7(*e*). The structures are much larger than those observed for FC-72 at the same frequency (compare figures 3*c* and 7*d*) due to the larger surface tension of water.

The periodic pattern evolution shown in figures 7(*a*)–7(*c*) is similar to the regimes observed by Ciliberto & Gollub (1985). These authors found that when the driving frequency and the driving amplitude are such that they lie in an overlap region of two modes (in their case modes (4,3) and (7,2) in water at a driving frequency $f = 16.1$ Hz and driving amplitude of about 2.5 times the threshold value of the sub-harmonic resonance modes), a periodic mode oscillation occurs. In a small region chaotic oscillations were also observed. At larger driving amplitudes the surface motion became chaotic at all driving frequencies investigated. Similar observations of axisymmetric waves modulated by parametric instability giving rise to lattice modes which again break down to random waves were also observed by Vukasinovic, Smith & Glezer (2007*a*) in drop atomization. We have not experimentally determined the phase diagram as was done for instance by Ciliberto & Gollub (1985) and by Das & Hopfinger (2008), because our aim has been to determine the pattern evolution for driving amplitudes leading to wave breaking and drop ejection at fixed driving frequencies. Nevertheless, it is of interest to determine the sub-harmonic resonance modes that are closest to the present driving frequencies in order to see whether the possibility that two modes overlap exists. From the dispersion relation (1.1) we get for water at the driving frequency $f = 50$ Hz a dimensionless wavenumber $kR = 15.81$ (where $R = 2.5$ cm is the container radius). The resonance modes are determined from the boundary condition, corresponding to $J_l'(k_{lm}R) = 0$, where the first index corresponds to the number of angular maxima.

The closest modes would be mode (4,4), corresponding to a driving frequency $f = 50.59$ Hz, and mode (14,1), corresponding to $f = 50.6$ Hz. However, these modes do not agree with observations (figure 7), and the number of radial wave crests would be incompatible with the container size. The other modes are mode (6,3) with $k_{63}R = 15.268$, corresponding to a driving frequency $f = 47.87$ Hz, and mode (9,2) with $k_{92}R = 15.286$, corresponding to a driving frequency $f = 47.94$ Hz. In principle, the frequency width $\Delta f$ over which instability occurs is too narrow (about 4 % at a forcing amplitude of about twice the critical value; see Ciliberto & Gollub 1985; Edwards & Fauve 1995) for these modes to include $f = 50$ Hz. It is known, and has been demonstrated by Das & Hopfinger (2008), that for water the frequency of a given wave mode is slightly higher than the theoretical value because the contact line is pinned and does not satisfy the theoretical boundary condition. (The effective container radius appears slightly smaller than the actual radius). This would shift the frequency of modes (6,3) and (9,2) sufficiently to the experimental driving frequency such that, at a driving amplitude of about twice the threshold value, the experimental driving frequency and amplitude lie within the bounds of the two modes. In figure 7(*a*), five to six angular spikes (angular maxima) can be identified near the centre, and in figure 7(*c*) there are at least nine spikes. Considering all the imperfections, this would suggest a mode oscillation similar to Ciliberto & Gollub (1985), except that in our case the frequencies of the two modes are very close and the driving frequency is situated slightly above and not in between the frequencies of the two modes. In figure 7(*b*) nearer the container wall, it might be possible to identify 10 angular maxima and 5 in figure 7(*a*). Hence, the pattern in figure 7(*a*) appears to be sub-harmonic of that in figure 7(*b*). However, if this were the case, pattern 7(*a*) would not be an unstable primary mode because the wave amplitudes in figures 7(*a*) and 7(*b*) are

similar. Therefore, the most likely explanation is an oscillation between modes (6,3) and (9,2).

No mode oscillations have been observed in any other case in the present study other than for water at 50 Hz. For instance the pattern at the surface of FC-72 forced at $f = 25$ Hz (figure 5) is initially circular (imposed by the container shape), and then, at a forcing amplitude of about twice the experimental threshold value, an azimuthal pattern appears with seven angular maxima. The dimensionless wavenumber at 25 Hz is $kR = 13.4$ that is close to mode (7,2) of $k_{72}R = 12.93$, corresponding to a forcing frequency of 24.44 Hz. Mode (8,2) would correspond to a forcing frequency of 25.8 Hz. The driving frequency of 25 Hz is thus within about 2 % of the frequency of mode (7,2) so that the unstable surface pattern is able to lock on to this mode when the driving amplitude is about twice the threshold value. The stability bound of (7,2) is crossed before the intersection of this bound with that of mode (8,2) so that no oscillation occurs. If an experimental driving frequency of 50.5 Hz would have been chosen, an oscillation between modes (7,2) and (8,2) could have been possible but difficult to identify unambiguously because of the closeness of the two modes. Note that with FC-72 the contact line is free to move so that the experimental boundary condition corresponds to the theoretical one.

For FC-72 at 50 Hz and water and FC-72 at 100 Hz the dimensionless wavenumbers are very large, and the wave patterns tend to become independent of the container shape. Also, far away from the instability bounds and irrespective of the pattern evolution it is found that the wave pattern consists of fluid cones moving laterally in a random fashion independent of the container shape.

We measured the distribution of the wavelengths of the crests at the drop ejection threshold for water from images similar to figure 7(*e*), where the crests and the troughs could be distinguished. The measurements were done by mouse clicks over the crests, using a program that captures the coordinates from mouse clicks. Data from three images were used to improve the statistics, and outliers were removed as per the criterion in Frank & Althoen (2002). Note that the images were acquired at half the forcing frequency, i.e. synchronous to the sub-harmonic parametric waves.

Figure 8 shows the probability density function of the wavelengths of crests at the drop ejection threshold, in the standardized form, for water at $f = 50$ Hz. The standard normal curve is shown as the solid line. The error bars represent the maximum possible error, corresponding to the size (0.6 mm) of the bright spots in figure 7(*e*). Repeated measurements from different image sets plotted in the figure show the possible vertical and horizontal variations of the data. The inset in figure 8 shows the normal probability plot of one of the data sets; linearity implies a normal distribution. The mean wavelength is $\lambda_m = 0.96$ cm with a standard deviation of $\sigma_\lambda \approx \lambda_m/5$. The mean wavelength is very close to the wavelength of 0.99 cm predicted by the dispersion relation. For capillary waves, the viscous instability analysis shows that the most unstable wavelength follows the inviscid scaling ($\lambda = C(\sigma/\rho)^{1/3}\omega^{2/3}$) obtained from the dispersion relation (Donnelly *et al.* 2004). This indicates that since the wavelengths at drop ejection are distributed normally around the sub-harmonic dispersion wavelength, the wavelength which becomes unstable first is predominant from the initiation of instability up to drop ejection. However, these sub-harmonic waves are superimposed with a large number of random waves with frequencies that are multiples of the sub-harmonic frequency. In other words, as wave turbulence is approached, the spectrum broadens but with a peak at the sub-harmonic frequency (Wright, Budakian & Putterman 1996). This spectral peak is eliminated in randomly forced wave turbulence (Falcon, Laroche & Fauve 2007).

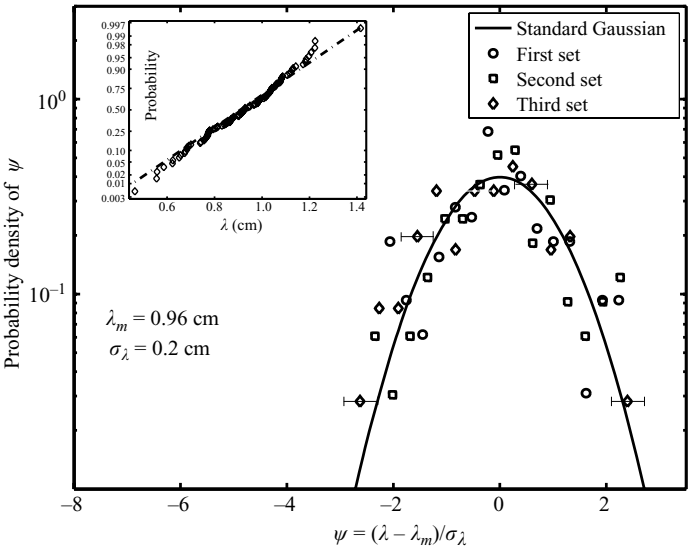


FIGURE 8. Distribution of wavelengths of the crests at drop ejection in water at $f = 50$ Hz for three sets of images. The inset shows the normal probability plot of the wavelengths for the third set. The mean wavelength of 0.96 cm is close to the wavelength of 0.99 cm obtained from the dispersion relation for sub-harmonic waves.

## 4. Drop ejection

### 4.1. *Characteristic scales*

Goodridge *et al.* (1997) found that drop ejection is essentially an inviscid process for dimensionless driving frequencies $\omega_\nu^* < 10^{-5}$, corresponding to $\omega < 10$ kHz for water and $\omega < 1$ kHz for FC-72. Hence, for low-viscosity liquids, in the frequency range 1–1000 Hz, the usual capillary–viscous scales are not the most appropriate scales to use.

We therefore propose a gravity–capillary scaling which gives dimensionless parameter values of order 1 in this low-frequency range. These frequency and length scales are respectively

$$\Omega_g = \left(\frac{g^3}{\sigma/\rho}\right)^{1/4} \text{ and } L_g = \left(\frac{\sigma/\rho}{g}\right)^{1/2}. \tag{4.1}$$

The resulting acceleration scale is $L_g\Omega_g^2 = g$. The dimensionless circular forcing frequency, forcing acceleration and forcing amplitude in the gravity–capillary regime are

$$\omega^* = \omega/\Omega_g, \tag{4.2}$$

$$a^* = a/g \quad \text{and} \tag{4.3}$$

$$A^* = A/L_g \tag{4.4}$$

respectively.

The dimensionless threshold acceleration is $a_d^* = a_d/g$. When the forcing frequency is sufficiently large ($\omega^* \gg 0.61$; see (4.21)), the drop ejection threshold should be independent of gravity, the only possibility that satisfies this condition is the power law

$$a_d^* = C_1\omega^{*4/3}. \tag{4.5}$$

| | $f$ (Hz) | $a_d$ (experiments) cm s$^{-2}$ | $a_d$ (1.5) cm s$^{-2}$ | $\omega_v^* \times 10^8$ | $\omega^*$ | $a_{vd}^* \times 10^{10}$ | $a_d^*$ ((4.5), $C_1 = 0.26$) |
|---|---|---|---|---|---|---|---|
| Water | 25 | 807.85 | 917.62 | 2.15 | 2.61 | 0.14 | 0.82 |
| | 50 | 1885.3 | 2312.3 | 4.3 | 5.22 | 0.45 | 2.68 |
| | 100 | 5160.8 | 5826.5 | 8.61 | 10.45 | 0.88 | 5.26 |
| FC-72 | 25 | 415.6 | 399.36 | 22.5 | 1.4 | 3.7 | 0.42 |
| | 50 | 983.6 | 1006.3 | 44.9 | 2.8 | 8.74 | 1.0 |
| | 100 | 2055.1 | 2535.8 | 89.83 | 5.6 | 18.26 | 2.09 |
| Glycerine–water | 50 | 12215 | 2045.6 | $3.8 \times 10^7$ | 4.77 | $4.27 \times 10^9$ | 12.45 |

TABLE 2. Droplet ejection threshold accelerations for the three fluids and the three driving frequencies plotted in figure 9. The measured accelerations are in column 3 and those predicted by (1.5) are in column 4. Columns 5–8 contain the dimensionless frequencies and accelerations, using viscous–capillary scales (subscript $v$) and gravity–capillary scales.

This expression is identical to (1.5) when $C_1 \approx 0.26$. In the other limit when wave breaking and drop ejection are dominated only by gravity, $a_d^*$ is a constant of the form

$$a_d^* = C_2. \tag{4.6}$$

The value of $C_2$ has not been determined. Expressions (4.5) and (4.6) suggest the general power law

$$a_d^* = C\omega^{*n}, \tag{4.7}$$

where $n$ and $C$ depend on the driving frequency with $0 \leqslant n \leqslant 4/3$. Wave breaking occurs when the dimensionless wave amplitude $b_d\omega_o^2/g = 1$, but the relation between $a_d$ and $b_d$ is not unique.

The crossover from gravity to capillary waves occurs at a wave frequency given by (1.2). The dimensionless forcing frequency corresponding to (1.2) is

$$\omega_t^* = 2\omega_{o_t}/\Omega_g = 2\sqrt{2}, \tag{4.8}$$

giving a convenient transition criterion from gravity to capillary waves. As will be seen below (§ 4.3.1), the crossover from gravity- to capillary-dominated breaking occurs at a different value of $\omega^*$, the difference being due to larger capillary effects because of a smaller radius of curvature of the wave crest.

### 4.2. *Drop ejection threshold*

Drop ejection is a continuous process. The ejection starts as very small droplets, ejected rarely, and increases with driving acceleration to larger drops ejected at a more uniform rate. Because of these initial rare drop ejection events, it is difficult to determine the drop ejection threshold acceleration accurately. Goodridge *et al.* (1997) defined the threshold acceleration by a criterion of two drops in 10 s. Here, we manually counted the number of drops ejected during a specific time period while increasing the driving acceleration by small increments. The measured drop ejection threshold shown in figure 9 corresponds to a drop ejection rate of 1 to about 16 drops in 30 s. The variation in acceleration encountered in this range of drop ejection rate was lower than the error involved in the measurement of the acceleration. Table 2 shows the values of the measured drop ejection threshold acceleration $a_d$ at three frequencies, for water, FC-72 and glycerine–water solution along with the values predicted by (1.5). There is reasonable agreement between the predicted and

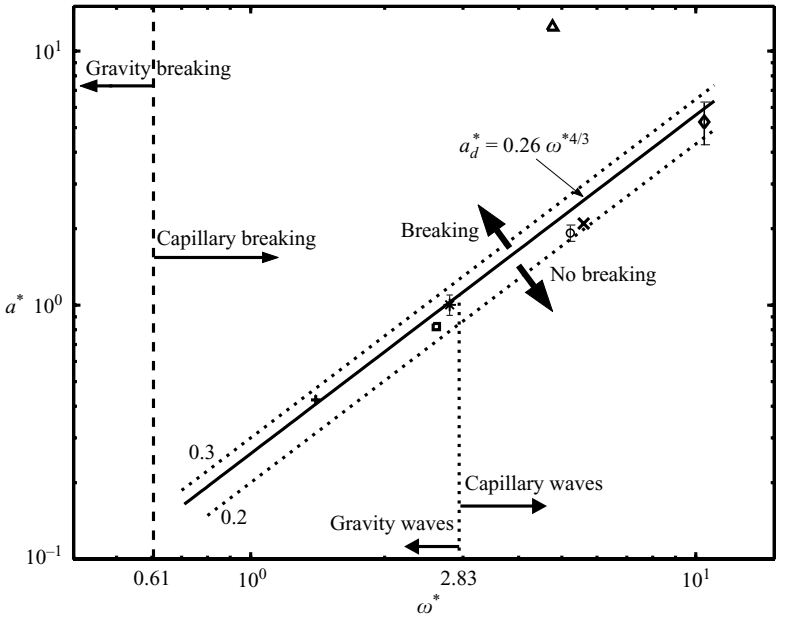


FIGURE 9. Variation of the drop ejection threshold acceleration with the forcing frequency, both non-dimensionalized by the gravity–capillary scales: +, FC-72 at $f = 25$ Hz; □, water at 25 Hz; ∗, FC-72 at 50 Hz; ○, water at 50 Hz; ×, FC-72 at 100 Hz; ◇, water at 100 Hz; and △, glycerine–water solution at 50 Hz. The solid line is (4.5) with $C_1 = 0.26$; breaking occurs above this line. Capillarity-dominated breaking occurs to the right of the dashed vertical line. The crossover from gravity to capillary waves is indicated by the dotted vertical line. The dotted lines parallel to the solid line show the maximum variation in the prefactor $C_1$ in (4.5).

experimental values. The table also shows the forcing frequency and the threshold acceleration, normalized by the viscous scales ($\omega_\nu^* = \omega/\Omega_\nu$ and $a_{\nu d}^* = a_d/L_\nu\Omega_\nu^2$) and the gravity–capillary scales ($\omega^* = \omega/\Omega_g$ and $a_d^* = a_d/g$). The gravity–capillary scales are more appropriate than the viscous scales, as the dimensionless driving frequencies and threshold accelerations are of order 1.

In figure 9, the dimensionless drop ejection threshold $a_d^*$ is plotted versus $\omega^*$ and compared with $a_d^* = 0.26\omega^{*4/3}$ (4.5). Breaking occurs if the point $(\omega^*, a_d^*)$ is above the solid line. The error bars shown are the larger of the two errors, viz. the error from repeated measurements and the error in calibration between the voltage input and the acceleration output of the shaker. The calibration error increases with acceleration as the deviation of the shaker performance from the linear calibration fit increases with increasing forcing amplitude. The vertical dotted line at $\omega^* = 2\sqrt{2}$ in figure 9 indicates the crossover from gravity to capillary waves according to (4.8), and the vertical dashed line indicates the crossover from gravity- to capillary-dominated breaking (4.21). All our data, except the high-viscosity glycerine–water data, agree with the inviscid scaling of (4.5). The variation in the prefactor $C_1$ in (4.5) that captures the data spread of the present experiments is approximately $0.26 \pm 0.05$. This variation is shown by the two parallel dotted lines in figure 9. The exponent $n$ in (4.7) has not been adjusted to experiments because a value of $n = 4/3$ is imposed by virtue of the assumption of capillary-dominated breaking (see § 4.1). However, we expect the value of $n$ to change from $n = 0$ when $\omega^* \ll 0.6$ (see § 4.3) to $n = 4/3$ when $\omega^* \gg 0.6$; i.e. $n$ is expected to be a function of the driving frequency in the frequency range of transition from gravity- to capillary-dominated breaking. It may be noted that the dimensionless

driving acceleration threshold value for the axisymmetric gravity wave is about 0.1 (Das & Hopfinger 2008) which is in agreement with figure 9.

### 4.3. *Relation between wave and container acceleration*

For capillary waves, Goodridge *et al.* (1997) quoted the wave amplitude at the drop ejection threshold as

$$b_d = 0.73\lambda. \tag{4.9}$$

Equating (1.5) to forcing acceleration $A_d\omega^2$ and using $\lambda$ from the dispersion relation, along with (4.9), the relation between the wave amplitude and the forcing amplitude $A_d$ at drop ejection threshold is

$$b_d \approx 28\, A_d\,. \tag{4.10}$$

The threshold capillary wave acceleration calculated from (4.10) using $\omega = 2\omega_o$ is seven times the forcing acceleration:

$$b_d\omega_o^2 \approx 7A_d\omega^2. \tag{4.11}$$

The relation between the wave and the forcing acceleration given by (4.11) can be obtained from a simple force balance model described below.

#### 4.3.1. *A physical model*

The model is based on the hypothesis that the capillary wave breaks (drop pinch-off at the wave crest) when the downward acceleration of the wave crest exceeds the downward acceleration due to the surface tension force. The surface tension force at the wave crest of radius $r$ is

$$F_\sigma = \frac{2\sigma}{r}S_c, \tag{4.12}$$

where $S_c = \pi r^2$ is the projected surface area. We assume that the mass to be accelerated to prevent breaking (drop detachment) is

$$m = K_1\,\frac{4}{3}\pi r^3\rho \tag{4.13}$$

with $K_1 \approx 0.5$ for a hemispherical cap. As the drop radius is generally larger than the wave crest radius just before breaking, we take

$$r \approx \frac{d}{2K_2} \tag{4.14}$$

with $K_2 > 1$, where $d$ is the mean drop diameter; $K_2$ is the ratio of the drop diameter to the wave crest diameter just before breaking. The present experiments suggest a value of $K_2 \approx 1.4$. In the numerical simulations of James *et al.* (2003*a*, figure 6), the ratio of the diameter of the drop that detaches (at their $t = 1.45$) to the wave crest diameter just before necking starts (at $t = 0.4$) is $1.25 < K_2 < 1.4$, depending upon where the wave crest radius is measured.

The drop diameter is expected to be proportional to the most likely wavelength at breaking. From ultrasonic atomization experiments, Lang (1962) determined the relation $d \approx 0.34\lambda$, where $d$ is the Sauter mean diameter and $\lambda$ the wavelength determined from the instability analysis. More recently, Donnelly *et al.* (2004) measured

$$d \approx 0.35\lambda \tag{4.15}$$

but using for $d$ the most likely drop diameter of the log-normal drop size distribution; the difference between the peak value and the Sauter mean diameter is 10 %–20 %.

Using (4.12)–(4.15) and the capillary dispersion relation for $\lambda$, in the expression for the downward acceleration $a_o = b_d\omega_o^2 = F_\sigma/m$, we get the threshold wave acceleration as

$$b_d\omega_o^2 \approx 4.86\,(\sigma/\rho)^{1/3}\,\omega_o^{4/3} \tag{4.16}$$

$$\approx 1.93\,(\sigma/\rho)^{1/3}\,\omega^{4/3}. \tag{4.17}$$

The wave acceleration is, therefore, 7.4 times larger than $a_d$ (1.93/0.26 from (4.17) and (1.5)), comparing favourably with (4.11).

The transition between gravity and capillary breaking can be determined from (4.16). At the drop ejection threshold, the relevant acceleration is the downward wave acceleration $a_o = b_d\omega_o^2$; gravity-dominated breaking occurs when this downward acceleration exceeds $g$ (Taylor 1953). Hence for gravity-dominated wave breaking, the threshold wave amplitude is

$$b_d = g/\omega_o^2 \tag{4.18}$$

$$= \lambda/(2\pi) = 0.16\lambda, \tag{4.19}$$

where we have used $\omega_o^2 = gk$ from the dispersion relation. For capillary wave breaking the threshold wave amplitude from (4.16) is

$$b_d = a_o/\omega_o^2 = 4.86\,(\sigma/\rho)^{1/3}\,\omega_o^{-2/3}. \tag{4.20}$$

Equating (4.18) and (4.20) we get the criterion for capillarity-dominated wave breaking as

$$\omega^* \geqslant 0.61. \tag{4.21}$$

This value is indicated by the vertical dashed line in figure 9. For FC-72, breaking is capillary dominated above $f = 10.9$ Hz, while for water, capillary-dominated breaking occurs above $f = 5.8$ Hz. The breaking threshold of gravity waves depends on the wave mode. Das & Hopfinger (2008) showed that for the axisymmetric mode, capillary effects remain important down to at least $\omega^* \approx 0.3$.

If $\omega_o$ on the right-hand side of (4.16) is expressed in terms of $\lambda$, given by the dispersion relation, we get

$$b_d\omega_o^2 \approx 19.4\pi^2\,(\sigma/\rho)\,\lambda^{-2}. \tag{4.22}$$

Using the wave acceleration calculated from (4.16) for water at $f = 50$ Hz, we obtain from (4.22) that $\lambda = 0.9$ cm, a value close to the most probable wavelength from the Gaussian distribution in figure 8. Also, if we substitute for $\omega_o$ from the capillary dispersion relation on the left-hand side of (4.22), we get $b_d \approx 0.77\lambda$ that is close to (4.9). According to (4.22), we expect the larger wavelength waves to be below the threshold wave acceleration and the smaller wavelength waves to generate spouts. It would also follow that waves with smaller wavelengths have larger amplitudes and vice versa. We now check these conjectures by observations of wave amplitudes at breaking.

Figure 10 shows the images of the wave heights near the drop ejection threshold for water and FC-72, obtained synchronous to the wave frequency. The undisturbed liquid level in all the images is 5 mm below the mark of 4 cm in the scale shown on the right-hand side of the images. Figure 10($a$) shows the wave heights at $\epsilon_d = (a - a_d)/a_d = 0.2$ for water at a forcing frequency of $f = 50$ Hz, where $a_d$ is given by (1.5). There is a distribution of wave heights, the peak being at 6 mm, that is, 1 mm above the 4 mm mark on the scale. Note that the shorter wavelengths have larger amplitudes, as predicted by (4.22). Figure 10($b$) shows the wave heights at the point of drop

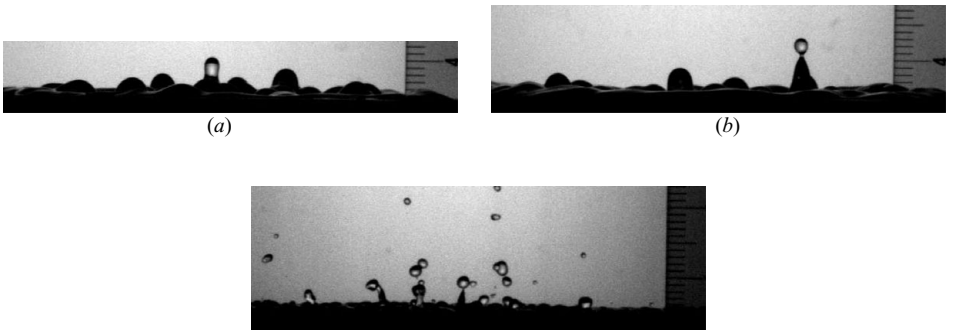

(*a*) (*b*) (*c*)

FIGURE 10. Wave heights near drop ejection. The undisturbed liquid level is at 3.5 cm on the scale shown at the right hand side of the images: (*a*) water, $f = 50$ Hz, $\epsilon_d = (a - a_d)/a_d = 0.2$; (*b*) water $f = 50$ Hz, $\epsilon_d = 0.5$; (*c*) FC-72, $f = 50$ Hz, $\epsilon_d = 1.2$.

formation for water, at $f = 50$ Hz, for a slightly higher forcing acceleration, $\epsilon_d = 0.5$. The wave height at the point of breaking and drop formation is about 6 mm. Figure 10(*c*) shows the wave heights at $\epsilon_d = 1.2$ for FC-72 at $f = 50$ Hz. Breaking occurs at a wave height of 3 mm. These measured heights correspond to $b_d/A_d = 26$ for water and $b_d/A_d = 29.4$ for FC-72, matching with the prediction of (4.10).

### 4.4. *Distribution of drop diameters*

Drop diameters have been measured previously in ultrasonic atomization in which viscous effects are of importance (Lang 1962; Donnelly *et al.* 2004) and in droplet atomization at around 1 kHz (Vukasinovic *et al.* 2004). No results seem to be available in the frequency range of order $10^2$ Hz. We determined the drop size distribution by image processing. The drop diameters were calculated from side view images, taken with the centreline of the camera aligned with the top of the container, similar to figure 10(*c*). The images were cut to the region above the container, and the background was then corrected to obtain bright drop images over a uniform dark background. A Canny edge detection routine, with an appropriate threshold level to discard diffuse edges due to unfocused drops, was used to obtain the white drop edges over a black background. Unconnected drop edges were connected by a bridging routine, and then the holes in the image (due to drops) were filled. Objects connected to the border were deleted to remove partial drops and the free surface of the liquid from the image. Objects with eccentricity greater than about 0.7 were discarded. This removed overlapping drops, jets and lines in the image. Isolated white pixels due to noise were then removed by a morphological opening of the image. The white regions in the image were then labelled and the areas of each label calculated. The drop diameters were calculated from the pixel areas of the drops using the scale factor for the images (0.09 mm pixel$^{-1}$). The statistics of the drop diameters at $f = 50$ Hz were calculated from 795 drops for water and from 1446 drops for FC-72, measured from about 400 images.

The present measurements of drop diameters are conducted at higher accelerations than the drop ejection threshold given by (4.5). The model presented in § 4.3.1 is valid only for the initiation of the drop ejection. At accelerations higher than the drop ejection threshold, at which we measure the drop diameters, the drops are mainly created by the breakup of ligaments. This can be observed in figure 11 which shows the production of drops in FC-72 and water at accelerations much higher than the drop ejection threshold. A similar ligament formation has been observed by Vukasinovic,

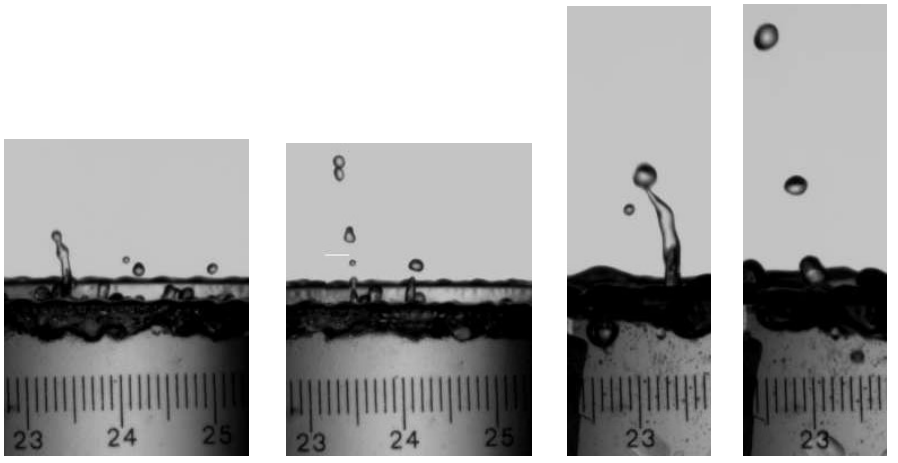


FIGURE 11. Drop ejection by ligament breakup at $f = 50\,\mathrm{Hz}$ when accelerations are higher than the drop ejection threshold. (*a*) Ligament formation in FC-72 at $\epsilon_d = 0.46$. (*b*) View after 1/30 s from (*a*). The ligament in (*a*) breaks into multiple small drops with a range of diameters. (*c*) Ligament formation in water at $\epsilon_d = 0.45$. The ligament is longer (compare *a* and *c*) and thicker than that in (*a*). (*d*) View after 1/30 s from (*c*). The ligament in (*c*) breaks, ejecting two drops of similar size.

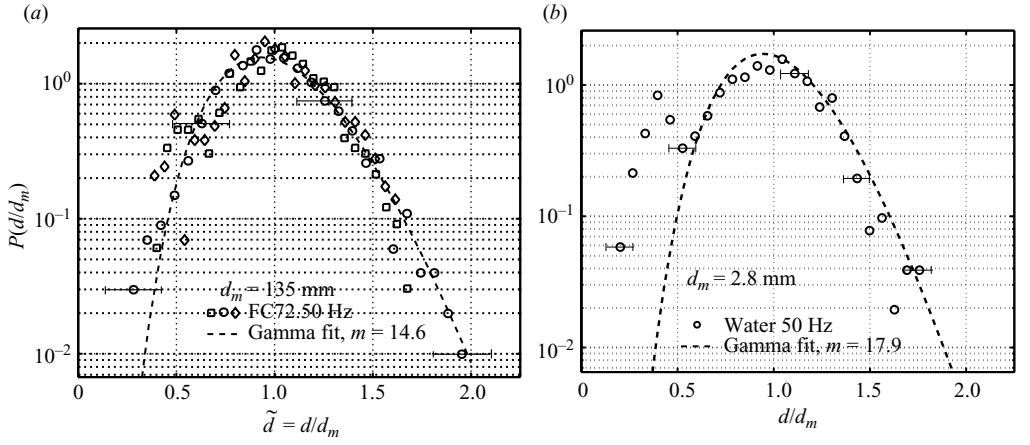


FIGURE 12. Probability distribution function of normalized drop diameters at $\epsilon_d \approx 1$: (*a*) FC-72, $f = 50\,\mathrm{Hz}$; (*b*) water, $f = 50\,\mathrm{Hz}$. The dashed line is the gamma fit. In comparison to water, drops ejected from FC-72 have a broader distribution of diameters with a smaller mean.

Smith & Glezer (2007*b*) in the case of drop atomization; these ligaments are caused by local cavity collapse. Hence, we compare our results with the ligament fragmentation theory of Villermaux (2007), which predicts a gamma distribution for the drop diameters. A log-normal fit also matched the present drop diameter distribution, as was the case with Donnelly *et al.* (2004). However, we present the gamma distribution, as it is consistent with the physical picture of drop formation by ligament breakup.

Figure 12 shows the probability distribution function of the normalized drop diameters $\tilde{d} = d/d_m$ for FC-72 and water at $f = 50\,\mathrm{Hz}$ and $\epsilon_d \approx 1$. The error bars are calculated by assuming $\pm 2$ pixel error in the edge detection. We consider the second peak in figure 12(*b*) to be the relevant drop diameter representative of the most likely

wavelength. The first peak of small drops is probably due to random events such as local cavity collapse or collision of the laterally moving wave crests. The mean drop size is $d_m = 1.35$ mm for FC-72 and $d_m = 2.8$ mm for water. The dashed lines in figure 12 (arithmetic mean) are the best fit standard gamma distribution curves of order $m$,

$$P(\tilde{d}) = \frac{m^m}{\Gamma(m)} \tilde{d}^{\,m-1} \mathrm{e}^{-m\tilde{d}}, \tag{4.23}$$

where $m = 14.6$ for FC-72 and $m = 17.9$ for water. As per Villermaux (2007), $m$ is the number of blobs of fluid in the ligament whose size is within $d$ and $d + \Delta d$ at time $t$. Larger $m$ implies longer, smoother and uniform ligaments breaking to give rise to narrower drop size distributions, while smaller $m$ implies barely elongated wave crests which break into few big drops and few small ones resulting in a broader drop size distribution. The distribution of FC-72 has a smaller $m$ and is broader than that of water. Since the surface tension of FC-72 is much lower than that of water we expect the ligaments to be less elongated than in water resulting in a broader drop size distribution.

These inferences match with the observations from the side view images of the liquid surface shown in figure 11. Figures 11($a$) and 11($b$) show the subsequent frames of the ligament breakup process in FC-72 at $\epsilon_d = 0.46$ and $f = 50$ Hz. Similar subsequent frames of the ligament breakup in water at $\epsilon_d = 0.45$ and same $f$ are shown in figures 11($c$) and 11($d$). Note that both the $\epsilon_d$ are calculated using $a_d$ given in table 2. The ligament in FC-72 is smaller in diameter and length compared to that in water; it breaks up to produce about four drops of a range of drop sizes. In the case of water, the ligament is thicker and longer than in FC-72. The ligament breaks up to produce two drops of larger size than in FC-72, these drops being of similar size. Such breakups result in a narrower drop size distribution with a larger mean drop size.

Since drop diameters do not depend on viscosity up to forcing frequencies of the order of kilohertz (Vukasinovic *et al.* 2004) and even megahertz corresponding to $\omega_\nu^* \sim 0.1$ (Donnelly *et al.* 2004), the drop diameter, made dimensionless by the gravity–capillary scales, can only depend on the dimensionless frequency, i.e.

$$d^* = C_3(\omega^*)^n, \tag{4.24}$$

where $d^* = d_m/L_g$. For breaking to be capillary dominated (gravity to be unimportant), $n = -2/3$. The mean drop diameters should thus scale as

$$d_m = C_3(\sigma/\rho)^{1/3}\omega^{-2/3}. \tag{4.25}$$

Similar scaling is obtained with capillary–viscous scales (1.6) and (1.7), as well as by assuming that the drop diameters are proportional to the wavelengths given by the dispersion relation for capillary waves. The value of the prefactors obtained from our experiments are $C_3 = 3.12$ for water and $C_3 = 3.44$ for FC-72. The variation of the prefactor is only 10 %, and the range includes the prefactor of 3.34 obtained by Donnelly *et al.* (2004). As per (4.25), the ratio of the drop diameters for water and FC-72, at the same driving frequency, should be equal to the ratio of $(\sigma/\rho)^{1/3}$ for the two fluids. The ratio of $(\sigma/\rho)^{1/3}$ for the two fluids is 2.3, and the ratio of the measured drop diameters is 2.1. The ratio of mean drop diameter to the mean wavelength for water at $f = 50$ Hz is 0.3 as against 0.35 from (4.15). Note that $d$ in (4.15) corresponds to the Santer mean diameter which is larger than the arithmetic mean diameter $d_m$.

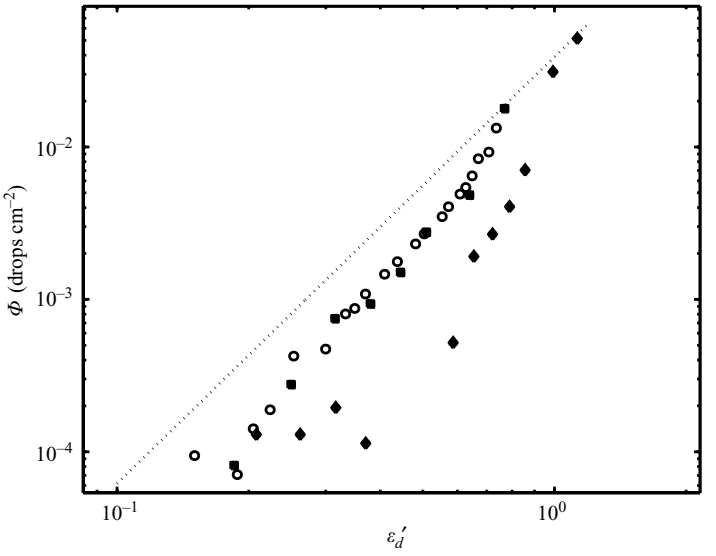


FIGURE 13. Variation of $\Phi$, the rate of drop ejection per unit area, with control parameter $\epsilon_d'$. The data points are the mean over repeated measurements: ■, water at $f = 50$ Hz; ◆, FC-72 at $f = 50$ Hz; ○, 100× glycerine–water (Goodridge *et al.* 1999) at $f = 45$ Hz; and $\cdots$, $0.039\epsilon_d'^{2.8}$.

### 4.5. *Drop ejection rate*

The drop ejection rate is difficult to determine accurately because the ejected drops may be counted twice, as the drops often fall back. The only measurements available are those by Goodridge *et al.* (1999) who used an expanded laser beam above the liquid surface. The number of drops crossing the beam were counted with a photodiode. Since the present experiments were not aimed specifically at measuring the flux of drops we did not develop an elaborate technique for measuring the flux. There is in fact no fully reliable technique of which we could think. We therefore used the simplest method available to measure the number of drops per unit time and projected surface area, that is by counting the number of ejected drops, $N$, at accelerations above $a_d$ in side view images. The images covered a region 7 cm in width and 3 cm in height above the wave surface $S$ with the total diameter of the tank within the depth of focus of the camera.

The images were acquired at 30 fps for a specific time period $T$ ($T = 10$ s for the lowest forcing accelerations and 0.5 s for the highest forcing accelerations). The measurements were repeated a few times at each acceleration. This technique was sufficient, as we limited our measurements to a small number of ejected drops (up to a maximum of six drops per image). Double counting due to drops falling back was avoided by counting only the drops that were travelling up. The drop ejection rate $\Phi$ per unit area is expressed by $\Phi = N/(ST\omega_o)$. For clarity, it may be noted that one drop ejected per wave period $2\pi/\omega_o = 0.04$ s corresponds to $\Phi = 0.008\,\mathrm{cm}^{-2}$. Goodridge *et al.* (1999) proposed for $\Phi$ the power law $\Phi = 0.039\epsilon_d'^{2.8}$, where $\epsilon_d' = (a - a_d')/a_d'$ and $a_d' = 0.8a_d$ with $a_d$ being the threshold drop ejection acceleration given in table 2 and shown in figure 9. At $a_d'$, that is about 20 % lower than the $a_d$ given in figure 9, intermittent but very rare drop ejection takes place. Figure 13 shows the variation of $\Phi$ with $\epsilon_d'$. The closed symbols represent water and FC-72 at $f = 50$ Hz, while the open symbol represent 100× glycerine–water data from Goodridge *et al.* (1999)

at $f = 45\,\mathrm{Hz}$. The expression $0.039\epsilon_d'^{2.8}$ is shown as the dotted line. Note that the experimental values of Goodridge *et al.* (1999, figure 2) do not match (1.11) or our data, unless multiplied by 100. Figure 13 indicates that the drop ejection rate is reasonably well represented by a power law when plotted against $\epsilon_d'$. If $\epsilon_d = (a - a_d)/a_d$ were to be used as the control parameter, no power law could be fitted. As has been pointed out by Goodridge *et al.* (1999) the large power in $\epsilon_d'$ is consistent with the extremely rare event of drop ejection at onset.

While the water and the FC-72 data follow a similar power law, their prefactors are different; in the case of water, more drops are ejected at the same value of $\epsilon_d'$. In an attempt to make the data collapse, a simple model is developed and outlined in Appendix B. At $a \gg a_d'$ drops are formed from ligaments or jets ejected from the fluid surface. These ligaments are a result of inertial collapse of cavities at some wave troughs. The diameter of these ligaments is then determined by the capillary wavelength, but the ligament spacing may be different. The number of drops per ligament is $N_l \sim L_l/d_m$, where $L_l$ is the ligament length and $d_m$ the mean drop diameter, proportional to the ligament diameter. The ligament length is to first order determined by inertial and gravitational force balance. This leads to (see Appendix B)

$$N_l \sim L_l/d_m \sim \epsilon_d'^2(a_d'/g). \tag{4.26}$$

The drop ejection rate is then $\Phi = N_l n_l$, where $n_l$ is the number of ligaments per unit area and dimensionless time $T\omega_o$. The functional dependence of $n_l$ on $\epsilon_d'$ may be assumed to be a power law and has, according to figure 13, a nearly linear dependence on $\epsilon_d'$ at least in the range of $\epsilon_d'$ investigated. In figure 14, $\Phi g/a_d'$ is plotted as a function of $\epsilon_d'$, and it is seen that (4.26) makes the data collapse quite well. The best fit for the rate of drop ejection per $\mathrm{cm}^2$ is

$$\Phi g/a_d' = 0.01\epsilon_d'^3. \tag{4.27}$$

In order to make $\Phi$ dimensionless a length scale is needed. One such length scale is the capillary wavelength and the other the gravity wavelength $\lambda_g = 2\pi g/\omega_o^2$. Since the ligament development depends on gravity, the more appropriate length scale seems to be $\lambda_g$ which is the same for water and FC-72. The ligament spacing is however a multiple of $\lambda_g$ because at the largest drop ejection rate considered, there are only one or two ligaments present at each period. If we define $\phi = \Phi(g/a_d')\lambda_g^2$, then the best fit of the data is

$$\phi = 0.0006\,\epsilon_d'^3. \tag{4.28}$$

The data would be well fitted by an exponential law of the form $\phi = \Phi\lambda_g^2 g/a_d = 8 \times 10^{-6}\exp(8.73\epsilon_d)$. If we use $\epsilon_d'$, then the exponential fit is $\phi = \Phi\lambda_g^2 g/a_d' = 1.75 \times 10^{-6}\exp(7\epsilon_d')$. Since we have no model or physical explanation for such an exponential behaviour, we did not present the data in this way. One of the referees pointed out that drop ejection is likely to be an activated process that would suggest an exponential dependency of $\phi$ on $\epsilon_d$. The power law model presented in Appendix B is an inertial–gravity model, which suggests a power law dependency of the ligament length on the forcing acceleration. However, the increase of the number of ligaments with $\epsilon_d$ might not follow a power law.

## 5. Conclusions and further discussion

The principal contribution of the present work is the gravity–capillary scaling that is more appropriate for low-viscosity fluids and forcing frequencies $f = \omega/2\pi < 1\,\mathrm{kHz}$.

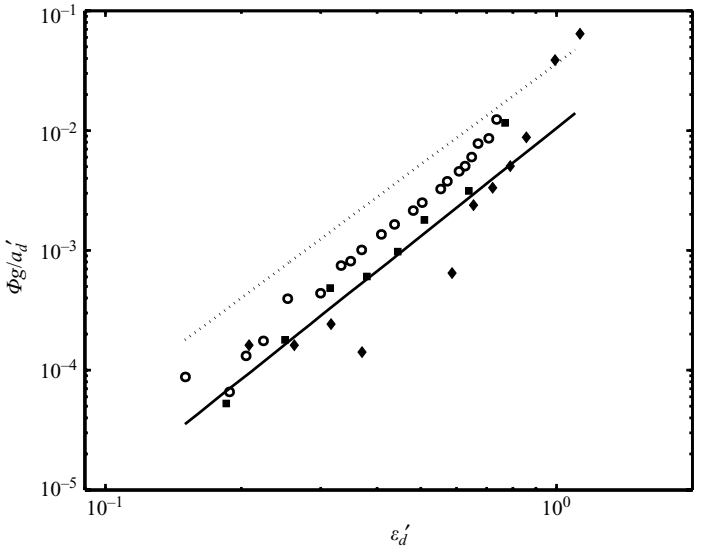


FIGURE 14. Variation of $\Phi$ scaled with $a_d/g$ with $\epsilon_d'$. The symbols are the same as in figure 13; $\cdots$, $0.036\epsilon_d'^{2.8}$; —, $0.01\epsilon_d'^{3}$

This scaling gives dimensionless acceleration ($a^*$, (4.3)) and frequency ($\omega^*$, (4.2)) values of order 1, and more importantly, it predicts the crossover from capillary wave breaking to gravity wave breaking (figure 9 and (4.21)). The threshold forcing acceleration for wave breaking is in the gravity wave limit $\omega^* \ll 0.6$, independent of forcing frequency. In the capillary-dominated range the threshold forcing acceleration $a_d$ has a power law $\omega^{*4/3}$ (4.5). In this limit $\omega^* > 0.6$, the present results, obtained with two liquids whose kinematic surface tensions differ by a factor of 10, are well fitted by a prefactor $C_2 \approx 0.26$ in (4.5), which is in agreement with the results of Goodridge *et al.* (1996). For a viscous liquid, the viscous scales $\Omega_\nu$ (1.6) and $a_\nu$ (1.8) must be used even at relatively low forcing frequencies. This is clearly seen in figure 9 in which the breaking acceleration threshold for glycerine–water solution ($\nu = 1.44\,\mathrm{cm^2\ s^{-1}}$) does not collapse on the inviscid law. The value of the dimensionless viscous forcing frequency $\omega_\nu^*$ (1.9) is of order 1 (0.38 at forcing frequency 50 Hz) for glycerine–water solution, whereas it is of order $10^{-9}$ for the low-viscosity liquids (see table 2). The crossover from viscous to inviscid breaking conditions is, according to Goodridge *et al.* (1997), at $\omega_\nu^* \approx 10^{-5}$. A condition for viscous effects to remain insignificant with respect to capillary effects is that the viscous length scale $(\nu/\omega_o)^{1/2}$ is much smaller than the capillary length scale $\sqrt{\sigma/(\rho a_o)}$, where $a_o$ is the wave acceleration at breaking, $a_o = 0.73\lambda\omega_o^2$. The ratio of viscous to capillary length scale is the capillary number, here equal to $Ca = \nu\omega_o^{1/3}/(\sigma/\rho)^{2/3}$. This number is of order $10^{-2}$–$10^{-3}$ for the low-viscosity liquids and about 1 for the glycerine–water solution. For the low-viscosity liquids, inertia dominates over viscous forces, the Reynolds number $Re = \omega_o\lambda^2/\nu$ being $10^3$–$10^4$. The Bond number $Bo = \rho\omega_o^2\lambda^3/\sigma \approx 10^2$. However, the wave crest radius is much smaller than $\lambda$ at breaking, giving a Bond number based on the wave crest radius of about 1. This force balance at the wave crest is expressed in the breakup model developed in § 4.3.1. It gives the relation between the container acceleration and the wave crest acceleration (4.17) and, consequently, the relation between the wave amplitude and the forcing amplitude. These results are of practical importance

because they give information about the fluid velocity for given vibration conditions, including horizontal vibrations.

The measured drop size distributions can be fitted by a gamma distribution with the mean drop diameter $d_m$ depending on the threshold wavelength (figure 8). The ratio $d_m/\lambda = 0.33 \pm 0.03$ is close to the value measured by Donnelly *et al.* (2004) in the ultrasonic frequency range in which the breakup process is dominated by viscosity. The distributions in the present experiments show a second peak of drop diameter about half the main peak. One explanation for this peak of lower diameters is the formation of jets due to collapse of cavities that have a smaller diameter than the retracting wave crest that forms the cavity. In ultrasonic atomization, viscosity may prevent this jet formation. As mentioned before, the drop size distribution is also well fitted by a log-normal distribution.

For low-viscosity fluids in small containers, the wave pattern near the instability onset is imposed by the container shape. With increasing forcing amplitude at a given forcing frequency, the observed pattern evolution is from circular waves that are azimuthally modulated to waves in the form of randomly moving fluid cones (when viewed from the top) at drop ejection (figure 3). The randomness of the wave motion at drop ejection has been pointed out by Yule & Al-Suleimani (2000). The wave pattern evolution shown in § 3 demonstrates that the waves become random well before drop ejection, even at values of $\epsilon = (a - a_c)/a_c \approx 0.25$ (see figure 4*b*); the specific value of $\epsilon$ depends on the fluid properties and the forcing frequency. These random waves are independent of container geometry, and the wavelengths between their crests can be approximated by a Gaussian distribution. The mean drop diameter scales with the threshold wavelength because the most probable wavelength of these random waves at drop ejection is practically the same as the threshold value.

The number of ejected drops above the drop ejection threshold was determined from side view images. Goodridge *et al.* (1999) measured the drop ejection rate in a viscous liquid (silicone oil) and suggested a correlation of the drop ejection rate per unit projected surface area $\Phi$ in terms of $\epsilon'_d = (a - a'_d)/a'_d$, where $a'_d = 0.8\, a_d$ is the threshold for rare, intermittent drop ejection. We find that drop ejection rate can be approximated by a cubic power law of $\epsilon'_d$. The dimensionless drop ejection rate $\phi$ as a function of $\epsilon'_d$ for the two liquids of very different surface tensions collapses reasonably well on a single curve when scaled by $a'_d/g$ as predicted by a model developed in Appendix B.

We wish to thank Pierre Carecchio and Joseph Virone, for their technical help. This work was financially supported by contract CNES/60167 within the French–German programme COMPERE.

## Appendix A. Laterally forced capillary waves

The general breaking criterion given by (4.16) should also hold for synchronous capillary waves, i.e. $\omega_o = \omega$. In order to verify this, we performed experiments with the same container vibrated in the horizontal direction. The vibration exciter was mounted with its spindle horizontal, and the Plexiglas container was screwed to the spindle through the side. The container was made perfectly horizontal by using an electronic level gauge.

We assume that the relation between the wave acceleration and the container acceleration, $b_d\omega_o^2 \approx 7A_d\omega^2$, still holds for synchronous waves. As the physical model of drop ejection in § 4.3.1 is valid for the case of horizontal forcing too, the wave

acceleration is given by (4.16). Using (4.10) and $\omega_o = \omega$, we get

$$b_d\omega_o^2 \approx 28A_d\omega^2 \approx 28a_d, \tag{A 1}$$

where $b_d\omega_o^2$ is given by (4.16). The threshold forcing acceleration for drop ejection in horizontal forcing is then

$$a_d = C_4\,(\sigma/\rho)^{1/3}\,\omega^{4/3} \tag{A 2}$$

with $C_4 \approx 4.86/28 = 0.17$. Note that this value is less than the value of 0.26 obtained for parametrically forced capillary waves. This inference matches our experimental observations of drop ejection condition for the horizontally forced case. From the threshold accelerations calculated from the horizontal forcing experiments, $C_4 = 0.169$ for water and $C_4 = 0.166$ for FC-72.

## Appendix B. Number of drops from a ligament

Neglecting the distribution of drop diameters as a first approximation, the number of drops from a ligament of length $L_l$ is

$$N_l \sim L_l/d_m, \tag{B 1}$$

where $d_m$ is the mean drop diameter. Assuming that the ligament length is determined by the balance of gravity and inertia, we get

$$L_l \approx V_o^2/(2g), \tag{B 2}$$

where $V_o$ is the fluid velocity at the base of the ligament. Here we have neglected the role of surface tension on the ligament development. This assumption is justifiable if the Bond number $Bo = \rho g L_l d_m/\sigma \gg 1$; $Bo \approx 8$ for water, while $Bo \approx 25$ for FC-72. Expecting inertial collapse of free surface troughs to create the ligaments, we take

$$V_o \sim (b - b_d)\omega_o, \tag{B 3}$$

where $b$ is the wave amplitude and $b_d$ the threshold drop ejection wave amplitude. The wave amplitude $b \sim a/\omega_o^2$, and since $d_m\omega_o^2 \sim a_d$ we get from (B 1)–(B 3)

$$N_l \sim \frac{(a - a_d)^2}{2a_d g} \sim \epsilon_d^2 \frac{a_d}{g}. \tag{B 4}$$

It is of course possible to replace $a_d$ by $a_d'$ in (B 4).

## REFERENCES

3M 2000 Fluorinert$^{TM}$electronic liquid FC72 product information sheet. *Tech Rep.* 3M Speciality Materials.

Batchelor, G. K. 1969 *An Introduction to Fluid Dynamics*. Cambridge University Press.

Bechhoefer, J., Ego, V., Manneville, S. & Johnson, B. 1995 An experimental study of the onset of parametrically pumped surface waves in a viscous fluid. *J. Fluid. Mech.* **288**, 325–350.

Benjamin, T. & Ursell, F. 1954 The stability of plane free surface of a liquid in periodic vertical motion. *Phil. Trans. R. Soc. Lond.* A. **225**, 505–515.

Binks, D., Westra, M. T. & Van de Water, W. 1997 Effect of depth on the pattern formation of Faraday waves. *Phys. Rev. Lett.* **79**, 5010–5013.

Chen, P. & Vinals, J. 1997 Pattern selection in Faraday waves. *Phys. Rev. Lett.* **79** (14), 2670–2673.

Ciliberto, S. & Gollub, J. P. 1985 Chaotic mode competition in parametrically forced surface waves. *J. Fluid. Mech.* **158**, 381–398.

Das, S. P. & Hopfinger, E. J. 2009 Mass transfer enhancement by gravity waves at a liquid-vapour interface. *Intl J. Heat Mass Transfer.* **52**, 1400–1411.

Das, S. P. & Hopfinger, E. J. 2008 Parametrically forced gravity waves in a circular cylinder and finite-time singularity. *J. Fluid. Mech.* **599**, 205–228.

Donnelly, T. D., Hogan, J., Mugler, A., Schommer, N. & Schubmehl, M. 2004 An experimental study of micron-scale droplet aerosols produced via ultrasonic atomization. *Phys. Fluids* **16** (8), 2843–2851.

Edwards, W. S. & Fauve, S. 1995 Patterns and quasi-patterns in the Faraday experiment. *J. Fluid. Mech.* **278**, 123–148.

Falcon, E., Laroche, C. & Fauve, S. 2007 Observations of gravity–capillary wave turbulence. *Phys. Rev. Lett.* **98**, 094503.

Frank, H. & Althoen, S. C. 2002 *Statistics, Concepts and Applications*. Cambridge University Press.

Gollub, J. P. & Meyer, W. 1983 Symmetry-breaking instabilities on a fluid surface. *Physica* D **6**, 337–346.

Goodridge, C. L., Hentschel, H. G. E. & Lathrop, D. P. 1999 Breaking Faraday waves: critical slowing of droplet ejection rates. *Phys. Rev. Lett.* **82** (15), 3062–3065.

Goodridge, C. L., Shi, T. & Lathrop, D. P. 1996 Threshold dynamics of singular gravity–capillary waves. *Phys. Rev. Lett.* **76** (11), 1824–1827.

Goodridge, C. L., Tao Shi, W., Hentschel, H. G. E. & Lathrop, D. P. 1997 Viscous effects in droplet-ejecting capillary waves. *Phys. Rev.* E **56** (1), 472–475.

Hopfinger, E. J. & Das, S. P. 2009 Mass transfer enhancement by capillary waves at a liquid-vapour interface. *Exp. Fluids* **46**, 597–605.

James, A. J., Smith, M. K. & Glezer, A. 2003*a* Vibration-induced drop atomisation and the numerical simulation of low frequency single-droplet ejection. *J. Fluid. Mech.* **476**, 29–62.

James, A. J., Vukasinovic, B., Smith, M. K. & Glezer, A. 2003*b* Vibration induced drop atomisation and bursting. *J. Fluid. Mech.* **476**, 1.

Jiang, L., Perlin, M. & Schultz, W. W. 1998 Period tripling and energy dissipation of breaking standing waves. *J. Fluid. Mech.* **369**, 273.

Jiang, L., Ting, C. L., Perlin, M. & Schultz, W. W. 1996 Moderate and steep Faraday waves:instabilities,modulation and temporal asymmetries. *J. Fluid. Mech.* **329**, 275.

Kudrolli, A. & Gollub, J. P. 1996 Patterns and spatiotemporal chaos in parametrically forced surface waves: a systematic survey at large aspect ratio. *Physica* D **97**, 133–154.

Kumar, K. & Tuckerman, L. S. 1994 Parametric instability of the interface between two fluids. *J. Fluid. Mech.* **279**, 49–68.

Lang, R. 1962 Ultrasonic atomization of liquids. *J. Acoust. Soc. Am.* **34**, 6–9.

Miles, J. & Henderson, D. 1990 Parametrically forced surface waves. *Annu. Rev. Fluid Mech.* **22**, 143–165.

Saylor, J. R. & Handler, R. A. 1997 Gas transport across an air/water interface populated with capillary waves. *Phys. Fluids* **9**, 2529.

Taylor, G. I. 1953 An experimental study of standing waves. *Proc. R. Soc.* A **218**, 44–59.

Topp, M. 1973 Ultrasonic atomisation-a photographic study of the mechanism of disintegration. *Aerosol Sci.* **4**, 17–25.

Villermaux, E. 2007 Fragmentation. *Annu. Rev. Fluid Mech.* **39**, 419–446.

Vukasinovic, B., Smith, M. K. & Glezer, A. 2004 Spray characterization during vibration-induced drop atomization. *Phys. Fluids* **16**, 306–316.

Vukasinovic, B., Smith, M. K. & Glezer, A. 2007*a* Dynamics of a sessile drop in forced vibration. *J. Fluid. Mech.* **587**, 395–423.

Vukasinovic, B., Smith, M. K. & Glezer, A. 2007*b* Mechanisms of free-surface breakup in vibration-induced liquid atomiation. *Phys. Fluids* **19**, 012104.

Wright, W., Budakian, R. & Putterman, S. 1996 Diffusing light photography of fully developed isotropic ripple turbulence. *Phys. Rev. Lett.* **76** (24), 4528–4531.

Yule, A. J. & Al-Suleimani, Y. 2000 On droplet formation from capillary waves on a vibrating surface. *Proc. R. Soc. Lond.* A **456**, 1069–1085.

Zhang, W. & Vinals, J. 1997 Pattern formation in weakly damped parametric surface waves. *J. Fluid. Mech.* **336**, 310–330.